Nanoscale

PAPER

View Article Online
View Journal

Cite this: DOI: 10.1039/d6nr00112b

Local strain-engineering of exciton energy in 2D materials with nanoindentation

Kristyna Yang,[a] Yucheng Yang,[a] Daniel A. Rhodes,[b] Katayun Barmak[b] and Matthew R. Rosenberger *[a]

Localized strain has emerged as a key parameter in locally tuning the electronic properties of 2D materials, including its role as a factor in the formation of single-photon emitters in 2D transition-metal dichalcogenides. While multiple studies have demonstrated the importance of localized strain, a quantitative understanding of how strain influences these optoelectronic phenomena and their properties remains incomplete, largely due to the lack of experimental approaches capable of applying large, well defined, localized strains. Here, we demonstrate that nanoindentation with spherical atomic force microscopy tips on polymer-supported 2D WSe_2 enables controlled application of large, local strain fields. Far-field photoluminescence spectroscopy reveals exciton energy red shifts of up to 0.29 eV, corresponding to maximum strains of 2.7% in the indent center, assuming −0.109 eV shift per % strain. By varying the indent depth, we achieve control over the strain magnitude, and by changing the spherical tip radius, we scale the spatial extent of the strained region. Combined with the deterministic positioning capability of atomic force microscopy, this method provides a precise and versatile platform for studying strain-dependent phenomena in 2D materials.

Received 9th January 2026,
Accepted 6th February 2026

DOI: 10.1039/d6nr00112b

rsc.li/nanoscale

Introduction

In recent years, two-dimensional (2D) Transition Metal Dichalcogenides (TMDs) have been studied for their extraordinary mechanical, electronic, and optoelectronic properties. Owing to their ultrathin nature and high mechanical strength, 2D TMDs exhibit remarkable strain tolerance and the ability to undergo significant out-of-plane deformations.[1] This ultrathin structure also enables extensive tunability of their optoelectronic properties through strain,[2–5] opening possible applications as hosts for electronic and optoelectronic devices.[6–8] Localized straining of 2D TMDs causes localized changes in the bandgap, a phenomenon explored in previous studies using methods such as naturally formed gas bubbles[9] and wrinkles,[10] draping over nanostructures,[10] and nano-indentation.[11,12] Though most of these methods lack precise control of the placement, extent, and magnitude of strain, nano-indentation stands out due to its high degree of control and reproducibility afforded by the high precision of the atomic force microscope (AFM).

Regardless, multiple studies have relied on uncontrolled or unmeasured localized strains to create prototype devices such as single photon emitters (SPEs) in monolayer (ML) WSe_2.[12,13] Recent studies indicate that the reliable creation of SPEs in ML WSe_2 requires the combination of a valley symmetry breaking defect[14] and a localized strain field.[15] In a 2019 study,[11] ML WSe_2 on a thin PMMA substrate was controllably indented with a sharp AFM probe, thus arbitrarily writing SPEs as a result of the highly localized strain from the indent.

Though the indentation method allows for control of the location and amount of sample deformation, through nanometer precise control of the x–y location and the depth of the indents, its limitation is the difficulty in quantifying the precise amount of strain applied and determining its spatial distribution. Previous attempts to model indents in ML/polymer samples have suggested that the highest magnitude strain occurs outside the area of the indent,[12] but due to the sharp AFM tips used for indentation, visualizing the details inside the indent remains challenging. Thus, it is still unknown what amount of strain is necessary for the formation of an SPE, how this strain affects the localized PL emission, and how tuning the strain magnitude may affect SPE properties.

Subsequent studies endeavored to understand further the formation of potential wells from nanoscale strain fields in randomly formed nano-bubbles[9] or on wrinkles caused by draping ML WSe_2 over nanostructures[10,16] – methods often used to induce localized strain. These studies measured photoluminescence shifts, which correspond to a localized bandgap

[a]Department of Aerospace and Mechanical Engineering, University of Notre Dame, Notre Dame, IN 46556, USA. E-mail: mrosenb2@nd.edu
[b]Department of Applied Physics and Applied Mathematics, Columbia University, New York, NY 10027, USA

minimum, using tip-enhanced spectroscopy[9,10,17] or far-field optical measurements at cryogenic temperatures.[16] This local band gap minimum is thought to contribute to the formation of SPEs. However, for better understanding and engineering of SPEs in ML WSe_2, there must be a reliable method for writing known, localized strains with arbitrary control of the strain %, placement, and spatial extent.

In this work, we create strained regions with spatial extent on the order of 1 μm in a ML WSe_2/polystyrene (PS) sample. By indenting a spherical AFM probe into the sample with controlled depth, we control the maximum strain and the size of the strained region. This results in a highly strained and unbroken region of ML WSe_2, with a localized PL redshift of up to 0.29 eV (corresponding to ~2.7% strain, assuming −0.109 eV shift per % strain[2]), which is clearly imaged by far-field PL spectroscopy at room temperature (RT). We demonstrate that the lowest energy peak position shifts linearly with respect to indent depth at both RT and 78 K. We show that the energy of the lowest energy peak is repeatable within approximately 0.01 meV when the peak energy is at 1.43 eV. Finally, we determine the maximum indent aspect ratio before material fracture and hypothesize that the magnitude of maximum strain is similar for indents with comparable aspect ratios, regardless of indent radius. This work provides a reliable approach for engineering strain profiles in 2D materials and decoupling the maximum strain magnitude and strain field spatial extent, paving the way for further studies into strain-tunable optoelectronic properties and device applications.

Results and discussion

AFM indentation with spherical probe

Despite the challenges of measuring and precisely varying the strain, nano-indentation is a highly controllable and repeatable method for creating localized strains.[11,12] Thus, we can build on the existing process to develop a system for writing large localized strains with the ability to control the strain magnitude, and clearly image the strained PL emission, to further study its effects in the formation of SPEs. The issues of an ambiguous strain profile and difficulty with controllably varying the strain in previous nano-indentation work are mainly due to the sharp probe, as after only a small displacement, the ML at the contact area fractures.[12] Thus, the highest strain is located near the polymer displaced around the indent rather than within the indent. However, if the AFM tip is large and smooth, it not only offers a clearer view of the deformation mechanics within the indent but also permits strain to be applied over a much larger area without causing material failure. Building on previous nano-indentation work, we used spherical AFM tips to develop an approach for writing arbitrary strains into a ML WSe_2/PS sample. Using this method, the highest strains are located at the bottom of the indent, and the PL shift due to the strain can be measured using conventional far-field PL spectroscopy.

Fig. 1 illustrates the mechanical process of introducing localized strains by AFM tip indentation. To create the sample, an exfoliated monolayer WSe_2 crystal is transferred onto a thin film of PS spun onto a Si wafer, using a gold-assisted exfoliation method.[18] detailed in the methods section. Then, an AFM probe with a large sphere on the tip is brought in contact with the sample surface, as shown in the experimental setup, Fig. 1a. The AFM probe is displaced by a certain displacement (z), thus deforming the PS into the shape of the sphere. When the probe is retracted, the PS retains the shape of the probe tip, and due to the adhesion between the monolayer WSe_2 and the PS surface, the ML holds the shape of the indent, creating a localized strain field.

The shape of an indent can be controlled by varying the size of the sphere tip and the amount of displacement, z, as shown in Fig. 1b. The plot shows the indent depth as a function of tip displacement for three different tip radii, R. All three data sets exhibit an approximately linear dependence on z until they reach a certain depth. After reaching this depth the slope of each data set changes and becomes steeper (indicated by the dashed ovals in Fig. 1b). This discontinuity in the data indicates the breaking of the ML WSe_2 as shown in the SI (Fig. S1 and S2) and further discussed in Fig. 3.

Fig. 1c–e show the AFM topography of three different indents made with a 1000 nm radius tip (R = 1000 nm) and increasing z from left to right. The line scan under each topography image shows the shape of the indent at its deepest point. The deformation around the edges of the indents is due to displaced PS. As shown in the line scans, the ML material inside the indent nominally conforms to the spherical tip shape without wrinkling, resulting in a smooth strain profile.

Spectroscopy of strained indents

Fig. 2 demonstrates that indentation can lead to large PL shifts which correspond to large localized strain.[2] Fig. 2a shows the AFM topography of a 101 nm deep, R = 1000 nm, indent into the WSe_2/PS sample. Fig. 2b shows individual spectra from the indent shown in Fig. 2a. The spectra are taken from different locations relative to the center of the indent, as labeled with triangles in Fig. 2a. The colors of the spectra in Fig. 2b correspond to the spatial location of the colored triangles in Fig. 2a.

Far from the indent (light blue spectrum), the PL spectrum is typical of unstrained WSe_2. In the middle of the indent (red spectrum), additional peaks appear with energy as low as 1.40 eV and the intensity of emission at the unstrained exciton energy (1.64 eV) is significantly decreased. Also, the energy of maximum emission occurs at around 1.60 eV. At points in between these two extremes, the spectra smoothly transition, as shown by the dark blue and purple spectra.

To interpret the spectra, we must consider the finite size of the laser beam used for the measurements because it is similar in size to the indent. The triangle locations are the nominal locations of the center of the laser spot during the spectroscopy measurements. The green dashed circle around one of the triangles indicates the extent of the laser spot,

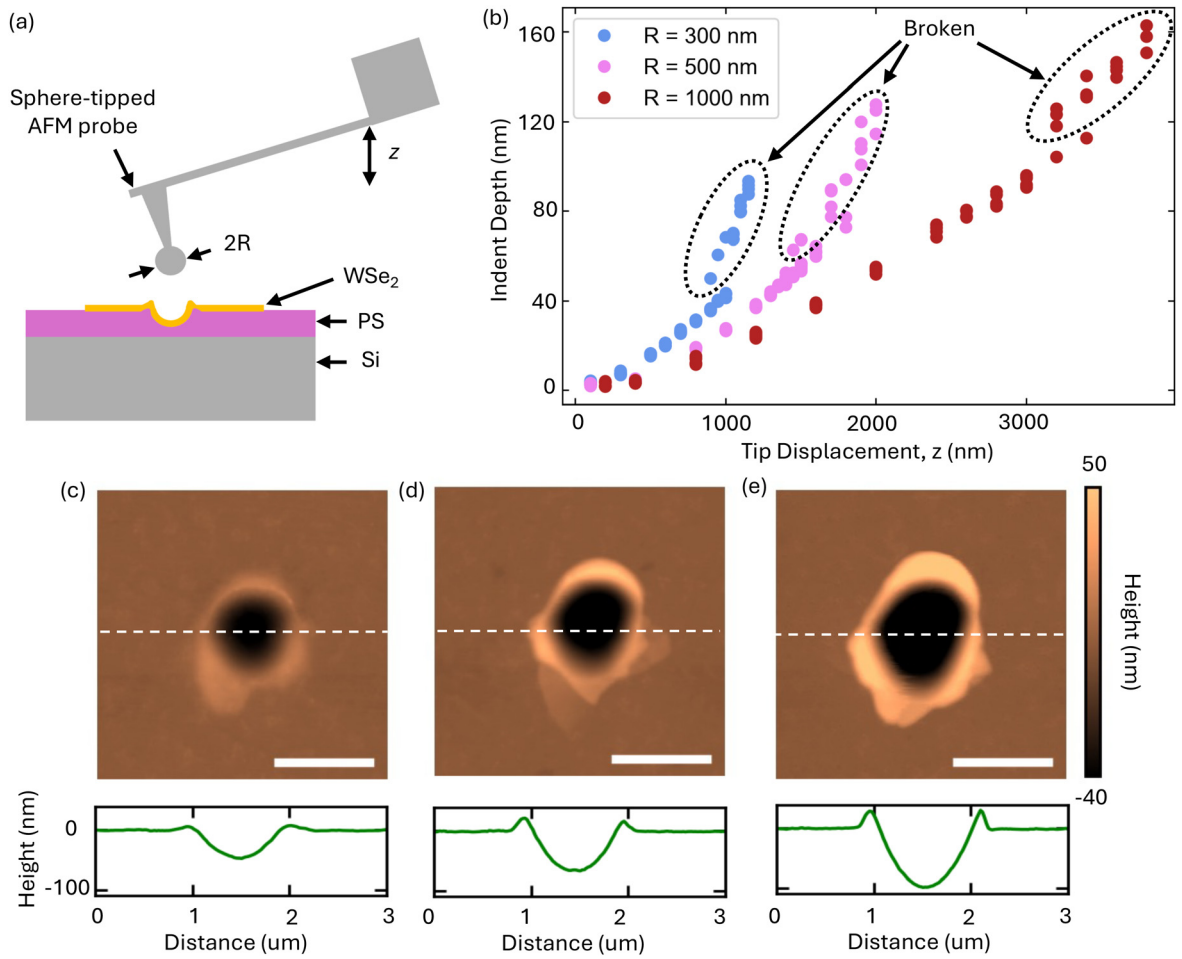

Fig. 1 (a) Schematic of the sample and indentation process. (b) Plot of indent depth *vs.* the tip displacement for tips with radii of 300 nm, 500 nm, and 1000 nm. (c–e) AFM topography of indents in WSe_2/PS sample created by a 1000 nm radius tip using 1600, 2100, and 2600 nm displacements, respectively. The dashed lines indicate the location of line scans directly below the topography images. All scalebars are 1 μm.

which was estimated from a line measurement across a Si/Gold edge (see SI Fig. S3). Each spectrum shown in Fig. 2b samples the area within the green dotted line around the pixel location shown in Fig. 2a. Thus, each PL spectrum is a superposition of emission from regions with different local emission characteristics, which are significantly modified by strain (later analysis provides evidence that strain is a dominant factor in the spectra).

The increasing intensity of emission below 1.45 eV near the bottom of the indent occurs because a larger portion of the laser spot is sampling a highly strained area. Notice that though the intensity of the unstrained neutral exciton decreases towards the indent center, it is still present in all spectra. We suspect this is because the laser is always sampling an area larger than the indent.

The increasing redshift happens because a higher strain results in a larger shift. Therefore, as the laser moves towards the center of the indent it is sampling higher strains until it reaches the center. The highest PL shift in Fig. 2b is about 0.25 eV relative to the position of the unstrained neutral exciton. The exact origin of the mid to low-energy emission possibly involves multiple excitonic contributions, and a more detailed discussion of these effects is presented in later sections.

Fig. 2c is a map of the integrated PL emission from 1.35–1.40 eV (the red shaded region in Fig. 2b) of the indent in Fig. 2a, showing the spatial distribution of the integrated PL intensity and the pixel locations of the spectra shown in Fig. 2b. The spatial distribution is approximately axisymmetric, consistent with the nominally axisymmetric shape of the indents.

Modulating maximum strain

Fig. 3 illustrates that the indent depth causes significant changes in the PL characteristics of the indents. In particular, the deeper indent depths result in a larger maximum PL energy shift and higher intensity emission below the unstrained neutral exciton energy.

Fig. 3a shows a typical spectrum from the center of a strained indent. The four shaded regions are centered around

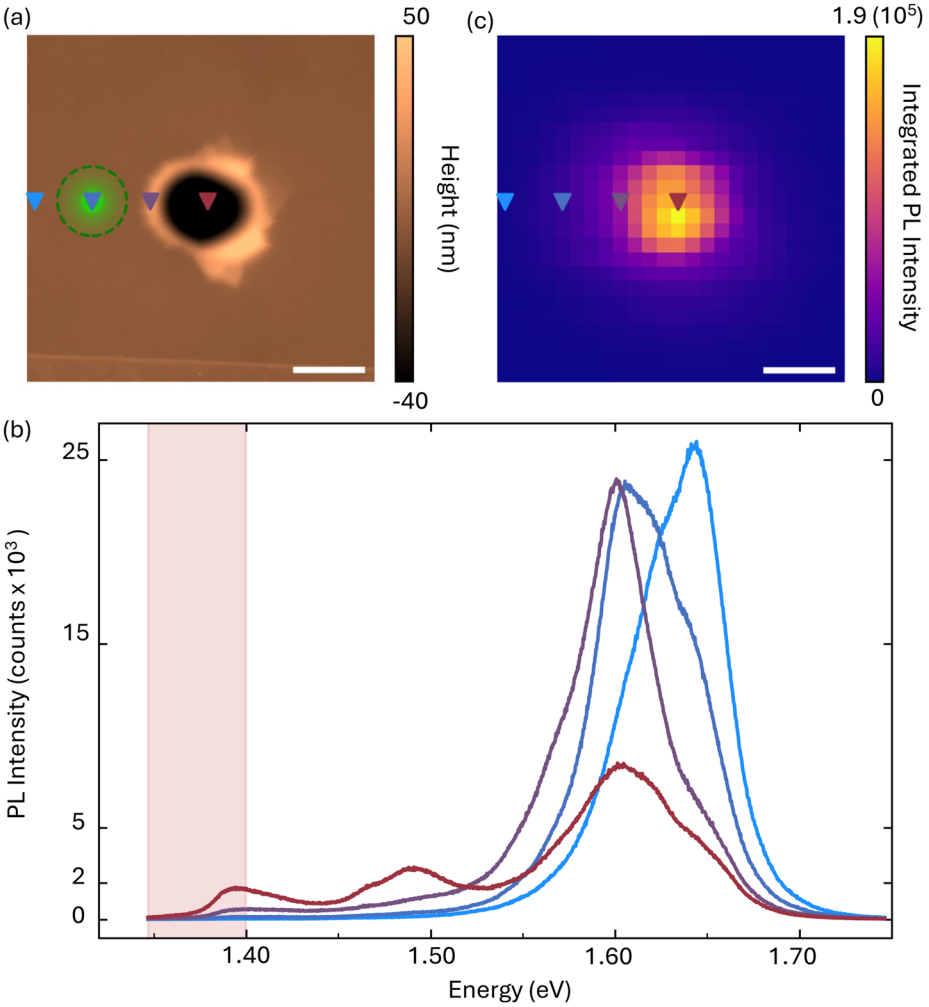

Fig. 2 (a) AFM topography of 101 nm deep indent. The green dashed line and green shading indicate the approximate size of the laser spot. (b) Plot of spectra approaching the indent center. Colors correspond to spatial markers in (a) and (c). (c) PL integrated intensity in the range 1.35–1.40 eV of the indent in (a). The shaded region indicates the range integrated in (c). All scalebars are 1 μm.

the locations of four noticeable peaks that are present to some degree in all the strained spectra. The blue range is centered around the location of the neutral exciton in the unstrained material. The green range is centered on the highest peak that emerges as the material is strained, from 1.55 to 1.63 eV. The yellow shoulder, which comes off the low end of the green region, and in some deep indents splits into two separate peaks, is typically centered anywhere between 1.45 and 1.55 eV. Finally, the deepest indents have a broad PL emission peak between 1.35 to 1.45 eV, in the red region.

Fig. 3b shows the spectra from three different indents with varying depths and one unstrained spectrum (from a flat region of the sample) for comparison. The three strained spectra were taken from nominally the same spatial location on the three different indents. An inset in Fig. 3b shows the location of the chosen spectrum on a map of the integrated PL intensity of an indent. The second inset in Fig. 3b is a close-up of the lower energy portion of the plot to better show the differences in low-energy emission. The indents used for Fig. 3b are shown in the AFM topography image in Fig. 3c, with their depths labeled.

Fig. 3d shows the PL integrated intensity maps of the indents in Fig. 3c for each shaded energy range in Fig. 3a. The four energy ranges exhibit different spatial distributions. The emission in the lowest energy range (red) is nominally in the middle of the indents and increases in intensity and spatial extent as the indents become deeper. The emission in the low intermediate energy range (yellow) is nominally in the middle of the indent for the shallowest indent and spreads away from the center of the indent in a three fold symmetry, consistent with the pattern of polymer displacement, as the indents become deeper. This evolution of emission pattern is consistent with a changing strain field as the indents become deeper. In particular, the region with strain that corresponds to the yellow spectral range increases in size and moves away from the center of the indents as the indent depth increases. The emission in the high intermediate energy range (green) exhibits an approximately donut shape that grows as indent depth

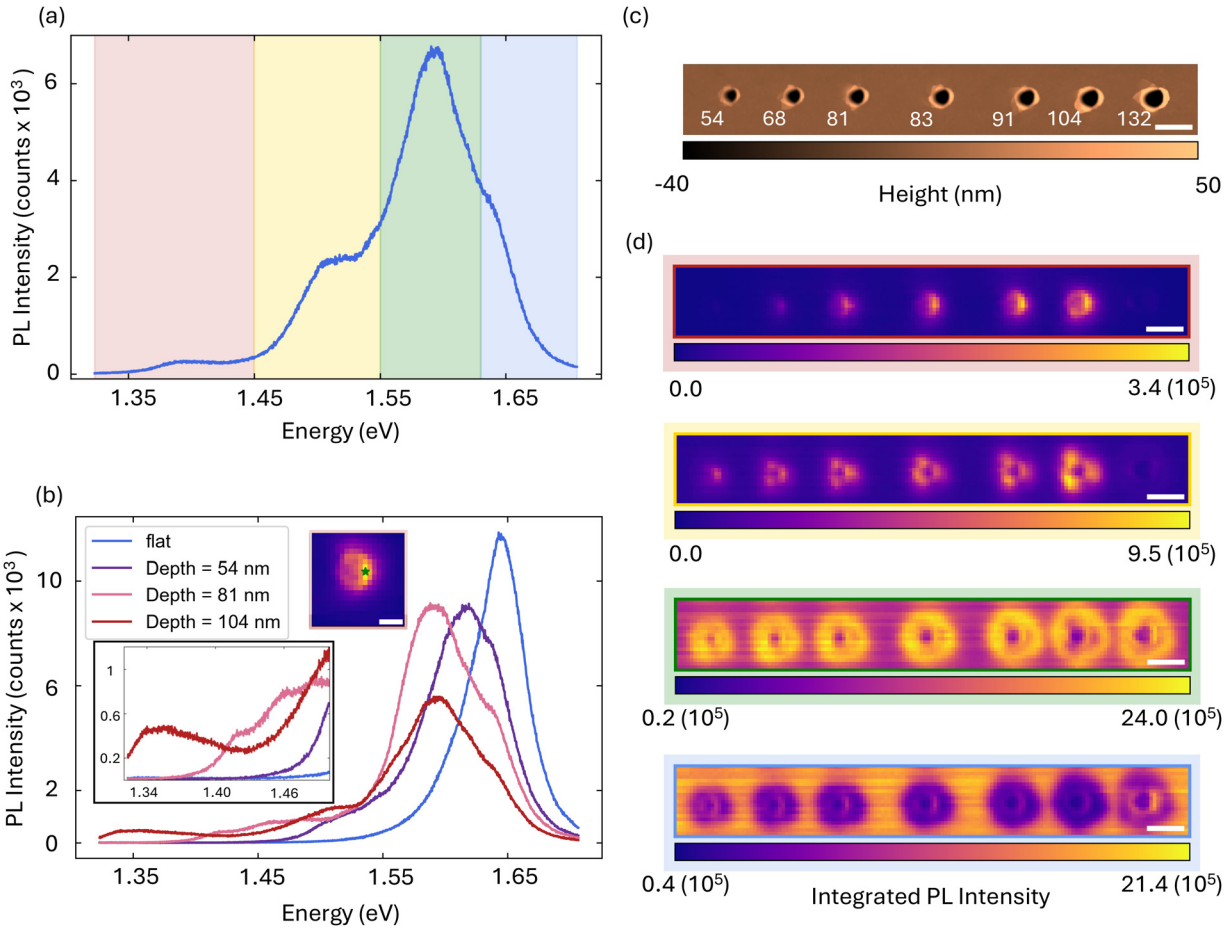

Fig. 3 (a) A typical PL spectrum in the center of an indent showing the four most common regions of PL emission peaks. Colors of shaded regions correspond to PL-integrated intensity maps in (d). (b) PL spectra from the same location of indents increasing in depth, as shown in (c). The inset shows the approximate location of the spectra on a typical indent PL map. Scalebar is 1 μm (c) AFM topography of sphere indents of increasing depth. Depths are labeled in nm. (d) PL-integrated intensity maps of indents in (c). The energy ranges integrated correspond to the colors of energy ranges shown in (a). Scale bars of (c) and (d) are 2 μm.

increases, also consistent with changing strain fields. Finally, emission in the unstrained neutral exciton energy range (blue) exhibits decreased intensity compared to the background, with the size of the reduced intensity region increasing with indent depth.

The maximum low-energy emission is expected to occur at the location of maximum strain, which would be centered in an ideal spherical indent. However, Fig. 3d shows that the PL intensity is instead localized along the right edge, indicating a non-ideal indent shape. For large-radius tips, a substantial force is required to initiate displacement of the PS substrate, causing the tip to initially slide forward as the indentation depth z increases and producing only a shallow indentation. As z increases further, the accumulation of displaced PS inhibits continued sliding, and the indent begins to deepen more rapidly. We were not able to mitigate this behavior by simply adjusting the indentation angle.

As a result, although indents produced using a R = 1000 nm tip exhibit smooth, approximately spherical profiles along the x-direction (Fig. 1c), the deepest region of the indent is shifted toward the front edge rather than being centered along the y-direction (see SI Fig. S4). As the tip radius is reduced, the indent profile along the y-direction becomes increasingly spherical as shown in SI Fig. S4.

It is important to note that the right most indent (134 nm) does not follow the previously discussed trends in Fig. 3d. It exhibits no emission in the red and yellow maps. In contrast, the green map shows the expected emission, while the blue map reveals a slight increase in neutral exciton intensity relative to the next deepest indent. This is because the ML WSe_2 inside the indent has broken, as discussed in Fig. 1b. As a result, emission in the red and yellow regions is absent because the bottom of the indent is relaxed. The increase in neutral exciton emission in the blue map is consistent with relaxation of the material at the indent center and the green map shows that the ML WSe_2 material outside the indent has not broken and is still strained.

All of the spectra shown in the figures in this work were taken the same day as the indents were made. We observe that emission in the red energy range decreases over time within

the first three or four days after indentation. This is attributed to the relaxation of the PS at the bottom of the indents where the tensile strain is at a maximum. Increasing the stability of the maximum strained region will be the focus of future work.

Quantitative analysis of spectral shifts

Even though Fig. 3 qualitatively demonstrates that both the PL integrated intensity and the special distribution of various regions of emission vary with indent depth, a quantitative comparison of the maximum strain requires quantitative analysis of the low-energy emission. To achieve this, we fitted every spectrum in a R = 1000 nm tip dataset using a combination of Voigt peaks, allowing us to systematically identify the position of the lowest-energy feature. As shown in Fig. 4a, each spectrum is decomposed into five Voigt peaks. This number of Voigt peaks was chosen because it produces the most accurate fit of the highest strain spectra for a wide range of indent depths. However, the focus of this work is the lowest energy peak, identified as p1 in Fig. 4a.

Fig. 4b shows the p1 peak energies for the R = 1000 nm dataset from Fig. 1b (excluding broken indents and indent depths <30 nm, see SI Fig. S5 and Table S1) as a function of indent depth. Data corresponding to indent depths <30 nm (shaded region) are omitted because such shallow indents do not exhibit a clearly identifiable p1. The data reveals a clear linear relationship between p1 energy and indent depth. This trend demonstrates that the location of the minimum energy peak (p1) is reliably controlled through indent depth.

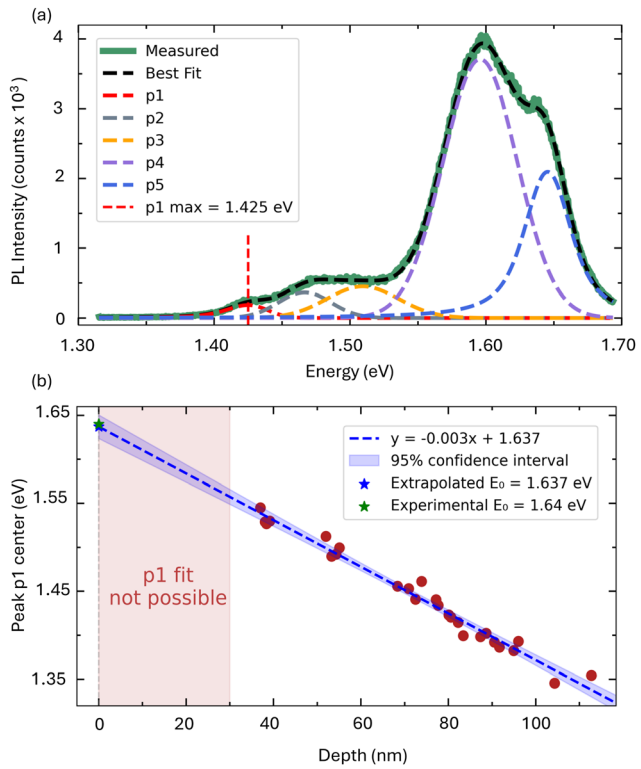

Fig. 4 (a) A strained spectrum from an R = 1000 nm indent, showing best Voigt Fit and individual components (p1–p5). The dashed vertical line marks the fitted p1 peak energy. (b) Extracted p1 energy as a function of indent depth for the R = 1000 nm indents shown in Fig. 1b, excluding indents with depths <30 nm and broken indents. The dashed blue line shows a linear fit of the data (with a 95% confidence interval of the linear regression). Extrapolation to depth = 0 gives the unstrained p1 energy (blue star). The experimental unstrained neutral exciton energy is plotted for comparison (green star).

The linear regression of p1 energy versus indent depth is shown by the blue dashed line in Fig. 4b, with the shaded region indicating the 95% confidence interval. Using this linear fit, we extrapolate to zero indent depth, which intuitively corresponds to the unstrained energy of the p1 feature. As indicated in the legend of Fig. 4b, the extrapolated unstrained p1 energy is 1.637 eV (blue star), while the experimentally measured unstrained neutral exciton energy of the sample is 1.64 eV (green star; see SI Fig. S6) and assuming a linear relationship between p1 energy and depth, it follows that the p1 feature originates at the same energy as the unstrained neutral exciton. We therefore conclude that the origin of the lowest-energy emission presented in this work originates from strained neutral excitons, although it may include additional complexities arising from the high localized strain gradients, the underlying mechanics of which have not yet been explored.

While not the focus of this work, the other peaks beside p1 warrant some consideration. First we note that emission below the unstrained neutral exciton can arise from a variety of excitonic species and excitonic complexes, most notably trions,[19] defect states[20,21], biexcitons,[21,22] phonon sidebands,[23,24] and dark excitons.[25] A common feature of these states is that they typically emerge most clearly at low temperatures and appear at energies relative to the neutral exciton that are determined by their respective binding energies.[26,27] Although trions and dark excitons have been observed at RT under the influence of localized strain gradients[28] or other doping mechanisms.[25,29,30]

Given the complexity of our measured spectra, it is likely that one or more of these excitonic species contribute to the broad emission observed between the neutral exciton and the lowest-energy feature. However, due to the complex strain field, the relatively large strain gradients, the laser spot size, broad linewidths at RT, and the strain-induced shift of the neutral exciton itself, a complete deconvolution of all contributing excitonic species is beyond the scope of this work and is left for future study.

Nevertheless, it is useful to highlight several probable origins of the most prominent spectral components. From right to left (high to low energy), p5 corresponds to the unstrained neutral exciton. We believe it is reasonable to assign the p4 peak to the trion, given the efficient conversion of excitons to trions induced by a localized strain gradient,[28] which explains the shift of the dominant emission peak from the neutral exciton energy to approximately 1.60 eV. The p3 and p2 peaks are attributed to localized exciton complexes.[19] Finally, the p1 peak, represents the lowest-energy emission

and is mainly attributed to the strained neutral exciton as described above.

The lowest p1 energy shown in Fig. 4b corresponds to an energy shift of 0.29 eV relative to the unstrained neutral exciton, which translates to a strain of 2.66% based on the strain – PL energy relationship reported in the literature.[2] This p1 energy is the lowest RT p1 emission energy reported in this work.

Repeatability of response

When applying large strains to investigate how strain magnitude influences PL phenomena, it is essential that both the indentation profiles and the resulting PL emission be repeatable. Fig. 5a shows the cross-sections of 11 indents made with a displacement z = 3000 nm on the same sample. The light red curves represent the raw indentation profiles, and the dashed blue line indicates their average. As illustrated, the indent shapes are consistent, with depths of 65 ± 3.1 nm and aspect ratios (depth/width) of 0.080 ± 0.003.

Although the indent geometries are highly repeatable, the more critical test of reproducibility is the comparison of the strained PL spectra across these 11 nominally identical indents. The key feature relevant to this study, the p1 energy associated with the maximum strain, should appear at a similar energy and magnitude.

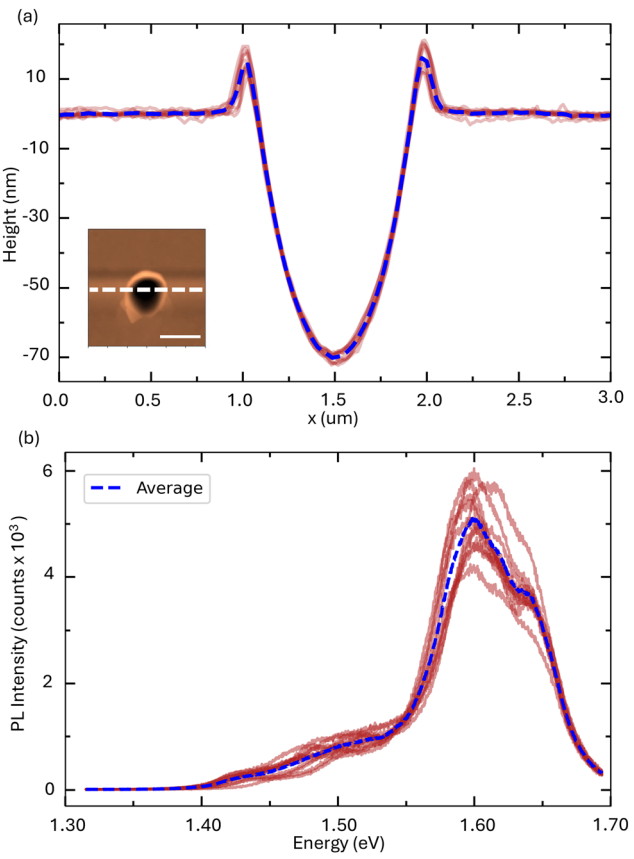

Fig. 5 Faded red lines represent raw data, and dashed blue lines show the average of all raw data for both (a) and (b). (a) A plot of 11 individual line scans of R = 1000 nm indents made with identical indentation parameters (z = 3000 nm). Inset shows the approximate location of the line scans on an example AFM topography image of an indent. (b) The plot of the maximum low energy spectra of the 11 indents from (a).

Fig. 5b shows the spectra of the pixel with the highest PL integrated intensity in the red shaded region (from in Fig. 3a) for each of the indents shown in Fig. 5a. The shaded curves show the raw data, and the dashed line is their average. Focusing on the p1 feature (fitted similarly to Fig. 4a) we find that the center energy of the fitted peak is 1.43 ± 0.01eV and the p1 peak amplitude is 184 ± 27 counts. These results indicate that the repeatability of the maximum strain for this indent depth is approximately 1.93 ± 0.1% strain.

Finally, it is important to emphasize that the repeatability of indents produced with identical displacement is ultimately limited by intrinsic variations within the ML WSe_2 and the underlying substrate. Additionally, the sample preparation process may introduce small, pre-indentation strains into the ML WSe_2 which is a normal part of the exfoliation and transfer. Thus, the baseline of the unstrained neutral exciton for different indents may vary slightly from indent to indent in both peak location and magnitude (SI Fig. S6).

Behavior at low temperature

We performed low-temperature photoluminescence measurements to examine how the strained regions behave at reduced temperatures. Although we do not have the capability to reach single-digit Kelvin, where most SPEs in ML WSe_2 are typically observed, our setup does allow optical measurements as low as 78 K (nominally). Based on past work, SPEs have been observed at temperatures above 78 K.[31] Fig. 7a shows the spectra of a 0.114 aspect ratio indent (R = 1000 nm) collected at 78 K, the blue spectrum, and at RT, the red spectrum. Due to limited range of the spectrometer, the spectra were acquired in two separate energy ranges and combined in the plot to display the full emission profile.

It is well established that cooling ML WSe_2 below 100 K leads to linewidth narrowing and a pronounced blue-shift of PL emission.[32–34] Consistent with this behavior, Fig. 6a shows the neutral exciton blue-shifting from approximately 1.64 eV at RT to 1.72 eV at low temperature. The excitonic features immediately below the neutral exciton also blue shift and remain overlapping with the neutral exciton. However, a distinct peak appears in the 1.30–1.40 eV range, corresponding to the approximate location and shape of the p1 feature at RT, so we assign this peak as p1.

Fig. 6b presents the spectra in the p1 energy range for indents of increasing aspect ratio at low temperature. Each spectrum has been shifted vertically, multiplied for clarity, and x-markers denote the p1 peak positions obtained from Voigt fitting. The p1 energy of the shallowest indent (light blue), which exhibits a slightly double-peaked structure, overlaps with the higher-energy peaks. As the indent aspect ratio increases (bottom to top in Fig. 6b), the p1 peak systematically moves to lower energies and becomes resolved from the higher-energy emission. In the deepest indent (red spectrum),

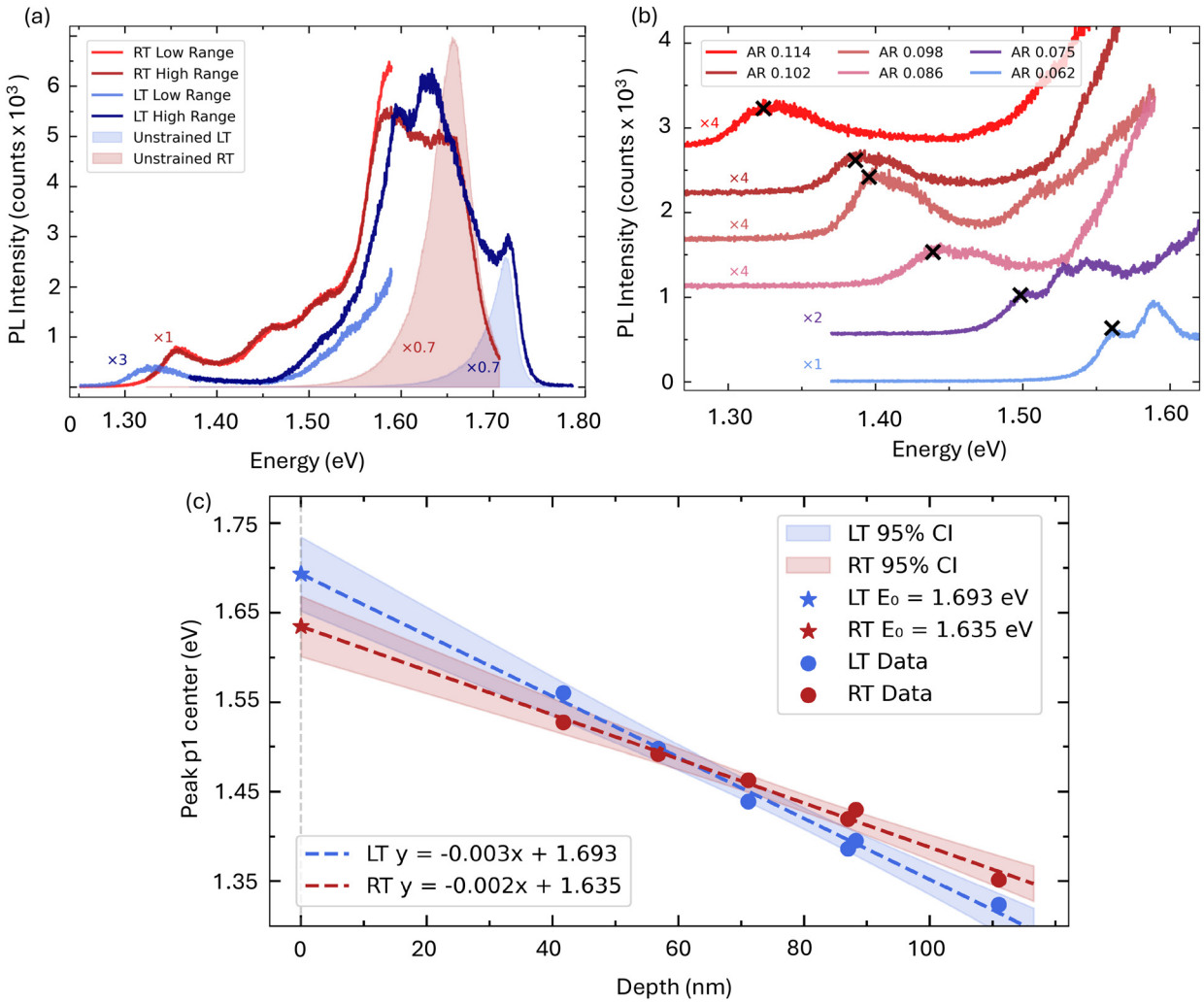

Fig. 6 (a) An example spectrum of a R = 1000 nm indent at RT (red spectrum) and 78 K (blue spectrum). The lightly shaded regions (red, blue) show the unstrained spectra (at RT, at 78 K). Spectra have been multiplied for clarity. (b) Plot of p1 region PL spectra at 78 K for R = 1000 nm indents with increasing ARs (depths). Spectra have been shifted vertically and multiplied for clarity. Black X marks the location of the p1 energy, from the Voigt fit shown in Fig. 4a. (c) Plot of p1 energy *vs.* indent depth for indents whose spectra are shown in (b), with linear fit. The blue data shows p1 at 78 K and red data show the p1 for the same indents at RT.

the p1 feature becomes fully isolated, as the intermediate region near 1.45 eV drops to the noise floor. The full spectrum for this indent is shown in Fig. 6a.

To more clearly illustrate this trend, Fig. 6c plots the p1 energy as a function of indent depth at RT (red) and at 78 K (blue) for the same set of indents. The dashed lines represent linear fits of each dataset, and the shaded regions their corresponding 95% confidence intervals. The linearity indicates that the p1 energy is strongly correlated with the indent geometry, and the extrapolation to the unstrained p1 energy yields similar results as Fig. 4b, namely that extrapolated p1 energy in the absence of indentation (zero strain) is in the region of the unstrained neutral exciton. This provides further evidence that p1 is related to the neutral exciton. The difference in the slopes of the RT and 78 K fits may result from several temperature-dependent changes such as a change in the strain response of PL emission, slight differences in the indent topography due to contraction of the polymer substrate, or enhanced exciton funneling and linewidth narrowing.

Further investigation of low-temperature strained indents is required to fully explain these observations. However, we suggest two compounding mechanisms that may contribute to the increasing separation of the p1 peak at lower temperatures. First, linewidth narrowing, experienced by multiple excitonic species at low temperature due to longer carrier lifetimes,[35] causes the feature to become more distinct. And second, increased exciton funneling efficiency at low temperatures[28,36] enhances carrier migration toward the highest-strain region. As a result, within the area sampled by the laser spot, the emission increasingly reflects only two dominant regions: the distant, unstrained background and the highly strained emis-

sion at the p1 location, with reduced contribution from intermediate strain regions.

Finally, we note that we did not observe sharp spectral features that would suggest SPE formation. This may be due to a lack of necessary defects in our samples[15,31] and will be the topic of future work.

Scaling of strained area

Fig. 7 shows that the area of maximum strain can be scaled by changing the tip radius while maintaining the value of maximum strain. Fig. 7a is a plot of indent aspect ratio (width/depth) versus tip displacement divided by tip radius for three different tip radii (see SI Fig. S7). The tip displacements range from zero to beyond the breaking point of the material for each radius tip. The data follows an approximately linear trajectory until reaching about 0.115 aspect ratio, denoted by the green line. After this, there is a discontinuity in the aspect ratio. All indents above the green line are indents where the material has broken. We determine that the indent is broken when the low-energy PL emission is missing, similarly to the broken indent shown in Fig. 3.

Fig. 7b shows the spectra of three separate indents made with the 300, 500, and 1000 nm tips, which all have the same aspect ratio of 0.10 and an unstrained spectrum for comparison. The inset in Fig. 7b shows the low energy range with the *y*-axis in log scale to better compare the low energy emission. The light blue spectrum, R = 300 nm, shows a slight hump at 1.53 eV whose tail extends to about 1.42 eV. The pink spectrum, R = 500 nm, has a peak around 1.47 eV, whose tail extends to 1.4 eV. Finally, the R = 1000 nm spectrum, red, shows a peak at 1.38 eV, whose tail extends past 1.35 eV.

Fig. 7c shows three PL maps of integrated intensity in the range 1.30–1.40 eV. Each map corresponds to a row of indents whose aspect ratios increase from 0 to the breaking point from left to right (this is the data displayed in Fig. 7a). The blue map shows indents of 300 nm radius, the pink map shows

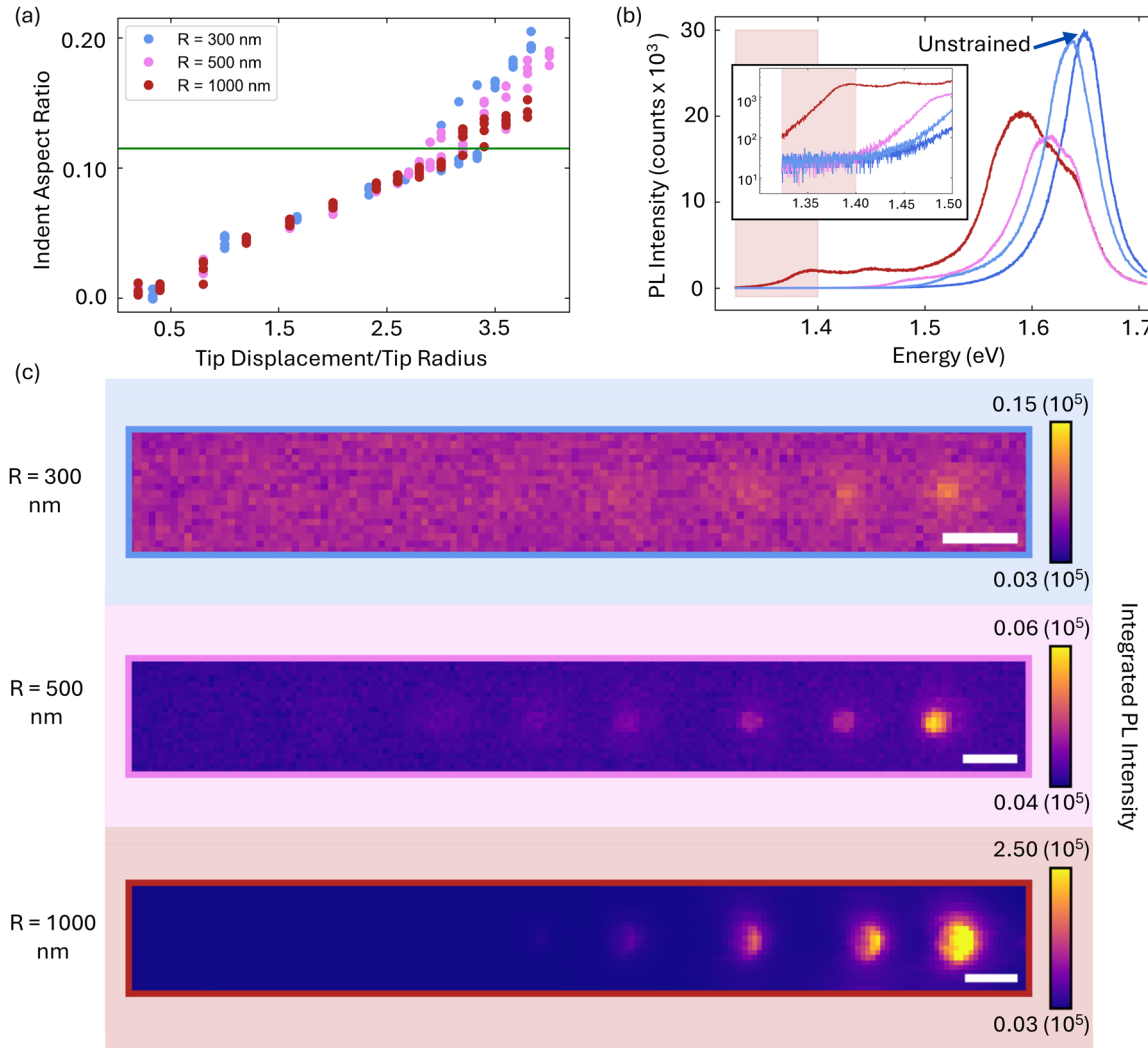

Fig. 7 (a) Plot of indent aspect ratio *vs.* tip displacement/tip radius for three different-sized tips. (b) Plot of spectra for 1000, 500, and 300 nm radius indents with an aspect ratio of 0.110. Inset of low energy range with *y*-axis in log scale. (c) PL-integrated intensity maps for three different-sized tips showing indents with aspect ratios ranging from 0–0.11 for each. All scalebars are 2 μm.

indents of 500 nm radius, and the red map shows 1000 nm radius indents.

The plot in Fig. 7a shows that the indent aspect ratio determines the material breaking point, not the indent depth. It is reasonable to assume that the material breaks when the maximum strain in the indent exceeds the breaking strain. We can infer, based on Fig. 7a, that spherical indents of the same aspect ratio have the same maximum strain. For simplicity we will assume the same spherical profile for all tip radius sizes. This is supported by models of strain in 2D material bubbles, such as the membrane approximation.[5,37,38] Under the membrane assumption, the maximum strain in a bubble, which is located at the bubble apex, is defined as

$$\varepsilon_{\max} = \sigma(\nu)\left(\frac{h}{a}\right)^2, \quad (1)$$

where $\sigma(\nu)$ is a constant dependent on the Poisson's ratio, ν, of the material, h is the bubble height, and a is the bubble radius. Therefore, smaller radius indents should have a similar maximum PL shift as the R = 1000 nm indents of the same aspect ratio. Because of the nature of our optical spectroscopy measurement, smaller indents show less low energy emission (due to the difference in indent area compared to the laser spot), and the maximum low energy emission may not be clearly visible above the noise of the measurement, as shown in Fig. 6b. Despite the measurement noise, the PL maps for both R = 500 and R = 300 nm, in Fig. 6c show an increase in integrated PL intensity from 1.30–1.40 eV for the indents on the far right. These indents have aspect ratios that are similar to the aspect ratios of the far right R = 1000 nm indents, which clearly show significant emission in the low energy range. This suggests that the maximum strain magnitude in the smaller radius indents is similar to R = 1000 nm indents of the same aspect ratios. This indicates that the area under maximum strain and the corresponding magnitude of the strain gradient can be scaled by changing the tip radius. However, more thorough measurements with a higher resolution strain measurement method are required to confirm this hypothesis.

Conclusions

In this work we have demonstrated a method for applying localized strain fields in a ML WSe_2/PS sample. We report low energy PL emission due to these strains up to 0.29 eV lower than the neutral exciton energy, and estimate a corresponding strain of about 2.7%. The shift of minimum PL energy, p1, is linear with respect to indent depth, establishing control of strain magnitude. Statistical analysis of the fitted p1 peak demonstrates that its unstrained energy coincides with the neutral exciton energy, providing strong evidence that the lowest-energy PL emission originates from strained neutral excitons. Furthermore, we show evidence that the maximum strain achievable is similar for different tip radii, which indicates that strain field size and corresponding strain gradients can be modified by changing tip radius while achieving the same maximum strain magnitude. The approach presented in this work provides a means to study the effects of strain magnitude and strain gradients on the behavior of various strain-dependent 2D material phenomena.

Methods

Gold assisted exfoliation

Monolayer (ML) WSe_2 was exfoliated from bulk crystals using the Au-assisted exfoliation method.[18] A 150 nm thick Au film was deposited onto a cleaned SiO_2/Si substrate *via* physical vapor deposition (PVD). A 1 : 20 solution of polyvinyl alcohol (PVA) in deionized (DI) water was then applied to the Au thin film and allowed to evaporate at 70 °C for 20 minutes.

Separately, bulk WSe_2 crystals were exfoliated using the 'scotch tape' method between two pieces of blue tape. Once the PVA layer had hardened, it was carefully separated from the SiO_2/Si wafer, lifting the Au thin film and exposing its previously uncontacted underside. The exfoliated WSe_2 on blue tape was then immediately brought into contact with the clean Au surface and firmly pressed. The PVA/Au stack was subsequently peeled away from the blue tape, ensuring that the Au thin film remained adhered to the PVA. This process facilitated the exfoliation of large ML WSe_2 crystals onto the clean Au surface.

Immediately after exfoliation, the PVA/Au stack was placed Au-side down onto a 523 nm thick polystyrene (PS) film, which had been spin-coated onto a SiO_2/Si wafer. The entire PVA/Au/WSe_2/PS/wafer stack was then submerged in DI water for several days to dissolve the PVA. Following PVA removal, the stack was submerged in gold etchant for 5 minutes to eliminate the Au layer and expose the ML WSe_2 on the PS surface. To ensure complete removal of residual PVA, the WSe_2/PS/wafer stack was further soaked in DI water for two days. Finally, the samples were indented and stored in a vacuum chamber for subsequent analysis.

Polystyrene substrates

To create the PS films a 5 wt% solution of polystyrene (MW 1200) (purchased from Scientific Polymer Products) and toluene (purchased from Sigma Aldrich) was spun onto a SiO_2/Si wafer piece (1.5 × 1.5 cm) using a spinner at 4000 rpm. The wafer piece was then annealed on a hot plate at 70° C for 1 minute to evaporate any residual solvent. The thickness of the PS film was then measured by scratching the film and using the AFM to measure across the edge. The PS films used in this work are all 523 ± 3 nm thick.

Crystal growth

WSe_2 crystals were grown using a self flux method with excess Se in a ratio of 1 : 15. Approximately 3 g total of W powder (99.999%) and Se (99.999%) were loaded into a quartz ampoule with an additional quartz wool just above the material and sealed under vacuum (~10^{-6} Torr). Subsequently the material was heated up to 1080 °C over 24 hours, held for

2 weeks, and cooled for 2 weeks down to 275 °C, where the ampoule was centrifuged to filter out the WSe_2 single crystals. As harvested crystals were subsequently resealed in quartz under vacuum and annealed with a temperature gradient of 275 °C at the WSe_2 position and the cold end at 175 °C to remove excess Se.

Optical spectroscopy measurements

All optical spectroscopy measurements in this work were performed on a Horiba Lab Ram Odyssey Raman Spectrometer with a 532 nm wavelength laser at room temperature. The laser power used was 0.82 μW and the accumulation time was 0.2 seconds.

AFM measurements

All AFM height measurements were made with the Horiba Smart SPM in tapping mode using a standard Si probe 100 nm long, purchased from BudgetSensors.

Nano-indentation parameters

The tips used for indentation were biosphere – B1000 – NCH, biosphere – B500 – NCH and biosphere – B300 – NCH purchased from NanoAndMore USA. The nano-indentation process was performed in the Horiba Smart SPM using the pre-installed curves_map macro in sweep Z mode. The feedback was in Sen mode. The indents were made at a displacement rate of 0.16 nm ms^{-1}. The optimal angle used to compensate for the sliding of the cantilever during indentation was found to be 23°. This was determined by varying the angle and comparing the shapes of indents with different angles but same displacement to find the most circular shaped indent. However, due to the large range of indent depths in this work, especially for the 1000 nm radius tips, the optimal angle for the deepest indents may not be exactly 23° thus the deepest of the 1000 nm radius indents are slightly asymmetrical. As can be seen in Fig. 3d and 4c. This skews the low energy PL emission slightly to one side due to the asymmetry of the deepest part of the indent. However, changing the compensation angle along with the indent depth is beyond the scope of this work. The compensation angle was kept at 23° for all indents.

Conflicts of interest

There are no conflicts to declare.

Data availability

The data supporting this article have been included as part of the supplementary information (SI). Supplementary information is available. See DOI: https://doi.org/10.1039/d6nr00112b.

Acknowledgements

KY, YY, and MRR acknowledge support from NSF DMR-2340398. This material is based upon work supported by the National Science Foundation Graduate Research Fellowship under Grant No. 1000315669. KB acknowledges support from NSF Materials Research Science and Engineering Center DMR-2011738. The authors acknowledge the help of Michael Grandel in the crystal growth.

References

1 E. Blundo, M. Felici, T. Yildirim, G. Pettinari, D. Tedeschi, A. Miriametro, B. Liu, W. Ma, Y. Lu and A. Polimeni, Evidence of the Direct-to-Indirect Band Gap Transition in Strained Two-Dimensional WS2, MoS2, and WSe2, *Phys. Rev. Res.*, 2020, **2**(1), 1–7, DOI: 10.1103/PhysRevResearch.2.012024.

2 Z. Li, Y. Lv, L. Ren, J. Li, L. Kong, Y. Zeng, Q. Tao, R. Wu, H. Ma, B. Zhao, D. Wang, W. Dang, K. Chen, L. Liao, X. Duan, X. Duan and Y. Liu, Efficient Strain Modulation of 2D Materials via Polymer Encapsulation, *Nat. Commun.*, 2020, **11**(1), 1–8, DOI: 10.1038/s41467-020-15023-3.

3 S. B. Desai, G. Seol, J. S. Kang, H. Fang, C. Battaglia, R. Kapadia, J. W. Ager, J. Guo and A. Javey, Strain-Induced Indirect to Direct Bandgap Transition in Multilayer WSe 2, *Nano Lett.*, 2014, **14**(8), 4592–4597, DOI: 10.1021/nl501638a.

4 A. M. Dadgar, D. Scullion, K. Kang, D. Esposito, E. H. Yang, I. P. Herman, M. A. Pimenta, E. J. G. Santos and A. N. Pasupathy, Strain Engineering and Raman Spectroscopy of Monolayer Transition Metal Dichalcogenides, *Chem. Mater.*, 2018, **30**(15), 5148–5155, DOI: 10.1021/acs.chemmater.8b01672.

5 D. Lloyd, X. Liu, J. W. Christopher, L. Cantley, A. Wadehra, B. L. Kim, B. B. Goldberg, A. K. Swan and J. S. Bunch, Band Gap Engineering with Ultralarge Biaxial Strains in Suspended Monolayer MoS2, *Nano Lett.*, 2016, **16**(9), 5836–5841, DOI: 10.1021/acs.nanolett.6b02615.

6 N. Huo, S. Yang, Z. Wei, S. S. Li, J. B. Xia and J. Li, Photoresponsive and Gas Sensing Field-Effect Transistors Based on Multilayer WS 2 Nanoflakes, *Sci. Rep.*, 2014, **4**, 1–9, DOI: 10.1038/srep05209.

7 M. Koperski, K. Nogajewski, A. Arora, V. Cherkez, P. Mallet, J. Y. Veuillen, J. Marcus, P. Kossacki and M. Potemski, Single Photon Emitters in Exfoliated WSe2 Structures, *Nat. Nanotechnol.*, 2015, **10**(6), 503–506, DOI: 10.1038/nnano.2015.67.

8 O. Iff, D. Tedeschi, J. Martín-Sánchez, M. Moczała-Dusanowska, S. Tongay, K. Yumigeta, J. Taboada-Gutiérrez, M. Savaresi, A. Rastelli, P. Alonso-González, S. Höfling, R. Trotta and C. Schneider, Strain-Tunable Single Photon Sources in WSe2 Monolayers, *Nano Lett.*, 2019, **19**(10), 6931–6936, DOI: 10.1021/acs.nanolett.9b02221.

9 T. P. Darlington, C. Carmesin, M. Florian, E. Yanev, O. Ajayi, J. Ardelean, D. A. Rhodes, A. Ghiotto, A. Krayev, K. Watanabe, T. Taniguchi, J. W. Kysar, A. N. Pasupathy, J. C. Hone, F. Jahnke, N. J. Borys and P. J. Schuck, Imaging Strain-Localized Excitons in Nanoscale Bubbles of Monolayer WSe2 at Room Temperature, *Nat. Nanotechnol.*, 2020, **15**(10), 854–860, DOI: 10.1038/s41565-020-0730-5.

10 E. S. Yanev, T. P. Darlington, S. A. Ladyzhets, M. C. Strasbourg, C. Trovatello, S. Liu, D. A. Rhodes, K. Hall, A. Sinha, N. J. Borys, J. C. Hone and P. J. Schuck, Programmable Nanowrinkle-Induced Room-Temperature Exciton Localization in Monolayer WSe2, *Nat. Commun.*, 2024, **15**(1), DOI: 10.1038/s41467-024-45936-2.

11 M. R. Rosenberger, C. K. Dass, H. J. Chuang, S. V. Sivaram, K. M. McCreary, J. R. Hendrickson and B. T. Jonker, Quantum Calligraphy: Writing Single-Photon Emitters in a Two-Dimensional Materials Platform, *ACS Nano*, 2019, **13**(1), 904–912, DOI: 10.1021/acsnano.8b08730.

12 A. N. Abramov, I. Y. Chestnov, E. S. Alimova, T. Ivanova, I. S. Mukhin, D. N. Krizhanovskii, I. A. Shelykh, I. V. Iorsh and V. Kravtsov, Photoluminescence Imaging of Single Photon Emitters within Nanoscale Strain Profiles in Monolayer WSe2, *Nat. Commun.*, 2023, **14**(1), 1–7, DOI: 10.1038/s41467-023-41292-9.

13 C. Palacios-Berraquero, D. M. Kara, A. R. P. Montblanch, M. Barbone, P. Latawiec, D. Yoon, A. K. Ott, M. Loncar, A. C. Ferrari and M. Atatüre, Large-Scale Quantum-Emitter Arrays in Atomically Thin Semiconductors, *Nat. Commun.*, 2017, **8**, 1–6, DOI: 10.1038/ncomms15093.

14 L. Linhart, M. Paur, V. Smejkal, J. Burgdörfer, T. Mueller and F. Libisch, Localized Intervalley Defect Excitons as Single-Photon Emitters in WSe2, *Phys. Rev. Lett.*, 2019, **123**(14), 146401, DOI: 10.1103/PhysRevLett.123.146401.

15 K. Parto, S. I. Azzam and K. Banerjee, Defect and Strain Engineering of Monolayer WSe2 Enables Site-Controlled Single-Photon Emission up to 150K, *Nat. Commun.*, 2021, 1–8, DOI: 10.1038/s41467-021-23709-5.

16 Y. Lv, M. Abid, H. H. Cheng, C.Ó Coileáin, R. G. S. Sofin, C. R. Chang and H. C. Wu, Strain-Dependent Optical Properties of Monolayer WSe2, *J. Phys. Chem. C*, 2023, **127**(46), 22682–22691, DOI: 10.1021/acs.jpcc.3c06393.

17 K. Hasz, Z. Hu, K. D. Park and M. B. Raschke, Tip-Enhanced Dark Exciton Nanoimaging and Local Strain Control in Monolayer WSe2, *Nano Lett.*, 2023, **23**(1), 198–204, DOI: 10.1021/acs.nanolett.2c03959.

18 F. Liu, W. Wu, Y. Bai, S. H. Chae, Q. Li, J. Wang, J. Hone and X. Y. Zhu, Disassembling 2D van Der Waals Crystals into Macroscopic Monolayers and Reassembling into Artificial Lattices, *Science*, 2020, **367**(6480), 903–906, DOI: 10.1126/science.aba1416.

19 G. Wang, L. Bouet, D. Lagarde, M. Vidal, T. Amand, X. Marie and B. Urbaszek, Valley Dynamics Probed through Charged and Neutral Exciton Emission in Monolayer WSe2, *Phys. Rev. B*, 2014, **90**(7), 075413, DOI: 10.1103/PhysRevB.90.075413.

20 S. Zhang, C. G. Wang, M. Y. Li, D. Huang, L. J. Li, W. Ji and S. Wu, Defect Structure of Localized Excitons in a WSe2 Monolayer, *Phys. Rev. Lett.*, 2017, **119**(4), 1–6, DOI: 10.1103/PhysRevLett.119.046101.

21 Y. You, X. Zhang, T. C. Berkelbach, M. S. Hybertsen, D. R. Reichman and T. F. Heinz, Observation of Biexcitons in Monolayer WSe 2, *Nat. Phys.*, 2015, 477–482, DOI: 10.1038/NPHYS3324.

22 E. J. Sie, A. J. Frenzel, Y. Lee, J. Kong and N. Gedik, Intervalley Biexcitons and Many-Body Effects in Monolayer MoS 2, *Phys. Rev. B*, 2015, **125417**, 1–8, DOI: 10.1103/PhysRevB.92.125417.

23 Z. Li, T. Wang, C. Jin, Z. Lu, Z. Lian, Y. Meng, M. Blei, S. Gao, T. Taniguchi, K. Watanabe, T. Ren, S. Tongay, L. Yang, D. Smirnov, T. Cao and S. F. Shi, Emerging Photoluminescence from the Dark-Exciton Phonon Replica in Monolayer WSe2, *Nat. Commun.*, 2019, **10**(1), 1–7, DOI: 10.1038/s41467-019-10477-6.

24 E. Liu, J. Van Baren, T. Taniguchi, K. Watanabe, Y. C. Chang and C. H. Lui, Valley-Selective Chiral Phonon Replicas of Dark Excitons and Trions in Monolayer WS E2, *Phys. Rev. Res.*, 2019, **1**(3), 1–7, DOI: 10.1103/PhysRevResearch.1.032007.

25 K. D. Park, T. Jiang, G. Clark, X. Xu and M. B. Raschke, Radiative Control of Dark Excitons at Room Temperature by Nano-Optical Antenna-Tip Purcell Effect, *Nat. Nanotechnol.*, 2018, **13**(1), 59–64, DOI: 10.1038/s41565-017-0003-0.

26 G. Wang, A. Chernikov, M. M. Glazov, T. F. Heinz, X. Marie, T. Amand and B. Urbaszek, Colloquium: Excitons in Atomically Thin Transition Metal Dichalcogenides, *Rev. Mod. Phys.*, 2018, **90**(2), 21001, DOI: 10.1103/RevModPhys.90.021001.

27 V. Funk, K. Wagner, E. Wietek, J. D. Ziegler, J. Förste, J. Lindlau, M. Förg, K. Watanabe, T. Taniguchi, A. Chernikov and A. Högele, Spectral Asymmetry of Phonon Sideband Luminescence in Monolayer and Bilayer WSe2, *Phys. Rev. Res.*, 2021, **3**(4), 1–7, DOI: 10.1103/PhysRevResearch.3.L042019.

28 M. G. Harats, J. N. Kirchhof, M. Qiao, K. Greben and K. I. Bolotin, Dynamics and Efficient Conversion of Excitons to Trions in Non-Uniformly Strained Monolayer WS2, *Nat. Photonics*, 2020, **14**(5), 324–329, DOI: 10.1038/s41566-019-0581-5.

29 Z. Wang, Y. Liu, D. Chen, Z. Wang, M. Asbahi, S. D. Rezaei, J. Deng, J. Teng, A. T. S. Wee, W. Zhang, J. K. W. Yang and Z. Dong, Nanocavity-Induced Trion Emission from Atomically Thin WSe2, *Sci. Rep.*, 2022, **12**(1), 1–8, DOI: 10.1038/s41598-022-20226-3.

30 D. Andres-Penares, M. K. Habil, A. Molina-Sánchez, C. J. Zapata-Rodríguez, J. P. Martínez-Pastor and J. F. Sánchez-Royo, Out-of-Plane Trion Emission in Monolayer WSe2 Revealed by Whispering Gallery Modes of Dielectric Microresonators, *Commun. Mater.*, 2021, **2**(1), 1–9, DOI: 10.1038/s43246-021-00157-8.

31 S. C. Gavin, H. J. Chuang, A. Dasgupta, M. Kar, K. M. McCreary, S. J. Lee, M. I. B. Utama, C. Zhou, X. Li, G. C. Schatz, T. J. Marks, M. C. Hersam, B. T. Jonker and

N. P. Stern, High-Temperature Single-Photon Emission From Covalently Functionalized van Der Waals Heterostructures, *Adv. Sci.*, 2025, **11319**, 1–11, DOI: 10.1002/advs.202511319.

32 A. Arora, M. Koperski, K. Nogajewski, J. Marcus, C. Faugeras and M. Potemski, Excitonic Resonances in Thin Films of WSe2: From Monolayer to Bulk Material, *Nanoscale*, 2015, **7**(23), 10421–10429, DOI: 10.1039/c5nr01536g.

33 C. Robert, D. Lagarde, F. Cadiz, G. Wang, B. Lassagne, T. Amand, A. Balocchi, P. Renucci, S. Tongay, B. Urbaszek and X. Marie, Exciton Radiative Lifetime in Transition Metal Dichalcogenide Monolayers, *Phys. Rev. B*, 2016, **93**(20), 1–10, DOI: 10.1103/PhysRevB.93.205423.

34 G. Moody, C. K. Dass, K. Hao, C. H. Chen, L. J. Li, A. Singh, K. Tran, G. Clark, X. Xu, G. Berghäuser, E. Malic, A. Knorr and X. Li, Intrinsic Homogeneous Linewidth and Broadening Mechanisms of Excitons in Monolayer Transition Metal Dichalcogenides, *Nat. Commun.*, 2015, **6**, 1–6, DOI: 10.1038/ncomms9315.

35 T. Godde, D. Schmidt, J. Schmutzler, M. Aßmann, J. Debus, F. Withers, E. M. Alexeev, O. Del Pozo-Zamudio, O. V. Skrypka, K. S. Novoselov, M. Bayer and A. I. Tartakovskii, Exciton and Trion Dynamics in Atomically Thin MoSe2 and WSe2: Effect of Localization, *Phys. Rev. B*, 2016, **94**(16), DOI: 10.1103/PhysRevB.94.165301.

36 J. Feng, X. Qian, C. W. Huang and J. Li, Strain-Engineered Artificial Atom as a Broad-Spectrum Solar Energy Funnel, *Nat. Photonics*, 2012, **6**(12), 866–872, DOI: 10.1038/nphoton.2012.285.

37 Z. Dai, Y. Hou, D. A. Sanchez, G. Wang, C. J. Brennan, Z. Zhang, L. Liu and N. Lu, Interface-Governed Deformation of Nanobubbles and Nanotents Formed by Two-Dimensional Materials, *Phys. Rev. Lett.*, 2018, **121**(26), 266101, DOI: 10.1103/PhysRevLett.121.266101.

38 K. Yue, W. Gao, R. Huang and K. M. Liechti, Analytical Methods for the Mechanics of Graphene Bubbles, *J. Appl. Phys.*, 2012, **112**(8), 1–8, DOI: 10.1063/1.4759146.